JACS
JOURNAL OF THE AMERICAN CHEMICAL SOCIETY
pubs.acs.org/JACS
Article

Role of Nanoscale Interfacial Proximity in Contact Freezing in Water

Sarwar Hussain and Amir Haji-Akbari*

Cite This: *J. Am. Chem. Soc.* 2021, 143, 2272−2284

Read Online

ACCESS | Metrics & More | Article Recommendations | SI Supporting Information

ABSTRACT: Contact freezing is a mode of atmospheric ice nucleation in which a collision between a dry ice nucleating particle (INP) and a water droplet results in considerably faster heterogeneous nucleation. The molecular mechanism of such an enhancement is, however, still a mystery. While earlier studies had attributed it to collision-induced transient perturbations, recent experiments point to the pivotal role of nanoscale proximity of the INP and the free interface. By simulating the heterogeneous nucleation of ice within INP-supported nanofilms of two model water-like tetrahedral liquids, we demonstrate that such nanoscale proximity is sufficient for inducing rate increases commensurate with those observed in contact freezing experiments, but only if the free interface has a tendency to enhance homogeneous nucleation. Water is suspected of possessing this latter property, known as surface freezing propensity. Our findings therefore establish a connection between the surface freezing propensity and kinetic enhancement during contact nucleation. We also observe that faster nucleation proceeds through a mechanism markedly distinct from classical heterogeneous nucleation, involving the formation of hourglass-shaped crystalline nuclei that conceive at either interface and that have a lower free energy of formation due to the nanoscale proximity of the interfaces and the modulation of the free interfacial structure by the INP. In addition to providing valuable insights into the physics of contact nucleation, our findings can assist in improving the accuracy of heterogeneous nucleation rate measurements in experiments and in advancing our understanding of ice nucleation on nonuniform surfaces such as organic, polymeric, and biological materials.

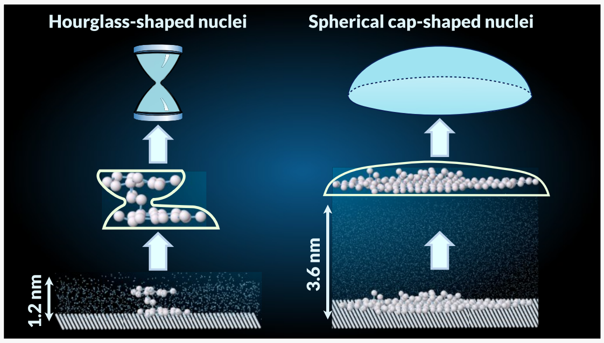

INTRODUCTION

Crystallization of liquids under nanoscale confinement has received considerable attention in recent decades,[1] as drastic changes in the thermodynamics of freezing,[2−7] the kinetics and mechanism of nucleation,[8−16] and the identity of the nucleated crystals[2,5,17] have been reported in numerous experimental[4,7,13,14,16] and computational[2,3,5,8−12,15,17] studies of freezing in nanopores,[7,13,14,16] nanotubes,[2,4,17] slit pores,[3,6] wedges,[15] nanodroplets,[9] and freestanding nanofilms.[8,10−12] What has received less attention is the freezing of liquids under mixed-interface confinement: i.e., when a liquid is sandwiched between a solid−liquid and a free interface. Mixed-interface confinement can emerge in many different environments and can dramatically affect the spatial heterogeneity and kinetic stability of the corresponding systems. Examples include the glass transition temperatures[18,19] and crystallization tendencies[20] of organic and polymeric films and the formation of low-dimensional ices on solid surfaces.[21−24] One process that can be strongly affected by mixed-interface confinement is atmospheric ice nucleation, which plays a pivotal role in cloud microphysics.[25] The dominant mode of ice formation in clouds is *immersion freezing* (Figure 1a), in which ice nucleates heterogeneously on an ice nucleating particle (INP) fully immersed within an atmospheric microdroplet.[26] INPs can, however, come into close proximity of free interfaces, which can in turn alter the kinetics and mechanism of nucleation in nontrivial ways. Considering the highly stochastic nature of immersion freezing,[27] such changes can, for instance, introduce large uncertainties into experimental estimates of immersion nucleation rates.

A more intriguing example is *contact freezing* (Figure 1b-,c) in which nucleation is triggered by a collision between a dry INP and a supercooled water droplet.[28] Contact freezing is usually orders of magnitude faster than immersion freezing, as has been demonstrated for a wide variety of INPs.[29−33] Pinpointing the molecular origin of this enhancement is, however, extremely difficult due to the transient nature of contact freezing. While earlier works had mostly attributed it to transient factors caused by the collision,[34−37] more recent studies point to the pivotal role of mixed-interface confinement. For instance, Shaw and Durant[29,30] observed that the kinetic freezing temperature in droplets that undergo repeated cycles of freezing and melting only depends on the proximity

Received: October 7, 2020
Published: January 28, 2021

https://dx.doi.org/10.1021/jacs.0c10663

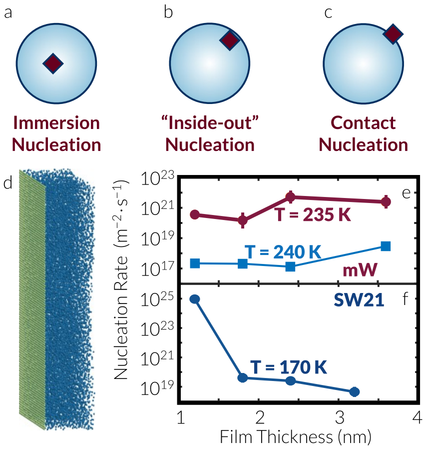

Figure 1. Free interfaces and the kinetics of heterogeneous ice nucleation. (a−c) Schematic representation of (a) immersion freezing, and (b) inside-out, and (c) conventional contact freezing, the three modes of heterogeneous ice nucleation discussed in this work. The INPs and water droplets are depicted in dark red and light blue, respectively. (d) Schematic representation of a graphene-supported thin film, with water molecules and carbon atoms depicted in dark blue and light green, respectively. (e, f) Dependence of heterogeneous nucleation rate on film thickness in (e) mW and (f) SW21 films. Error bars correspond to 95% confidence intervals and are smaller than the symbols.

of the INP and the free interface and is independent of whether the INP approaches the interface from the outside (Figure 1c) or from within (Figure 1b). These two modes of contact freezing are referred to as "outside-in" and "inside-out" freezing, respectively. Initially, it was argued that these observations might be explained by the supposed tendency of the water-vapor-INP contact line to facilitate nucleation.[38,39] Later experiments by the same group, however, found no such tendency[40,41] except for INPs with a nanoscale texture,[42] suggesting that nanoscale proximity might result in faster nucleation even in the absence of a contact line.

Despite these remarkable findings, there is a considerable gap in our understanding of how a vapor−liquid interface can enhance heterogeneous nucleation on a proximal INP. It has been argued[29,30,39] that this tendency might be linked to the suspected ability of a free interface to facilitate homogeneous ice nucleation. Here, "homogeneous nucleation" refers to nucleation in the absence of an extrinsic INP, whether it occurs in the bulk or is facilitated at the vapor−liquid interface. Surface-dominated homogeneous nucleation—typically referred to as *surface freezing*—was originally proposed by Tabazadeh et al.[43] and has since been extensively studied experimentally[44−46] and computationally.[8−12] Experimental evidence for surface freezing, however, is inconclusive mostly due to the difficulty of generating monodispersed droplets in the sub-micrometer size regime, where this effect is predicted to become dominant.[47] Computational studies of surface freezing have also been equally inconclusive,[48] as the enhancement of nucleation is only observed[8,11,12] for some force fields, such as the atomistic TIP4P/Ice[49] model, and not others,[9−11] such as the coarse-grained monoatomic water (mW)[50] potential. This force-field dependence of surface freezing propensity provides an opening for testing the hypothesized connection between free surface-induced homogeneous and heterogeneous nucleation, or surface and contact freezing, respectively. If such a relationship exists, the rate of heterogeneous nucleation in supported liquid nanofilms of a model prone to surface freezing will decrease drastically with film thickness, while no (or the opposite) dependence on thickness will be observed for the force field(s) with no surface freezing propensity.

Here, we use molecular dynamics simulations and our recently developed jumpy forward flux sampling (jFFS) algorithm[51] to test this hypothesis by computing the rates and characterizing the mechanism of heterogeneous nucleation in supported nanofilms of two model water-like tetrahedral liquids with opposing surface freezing propensities. Our focus on supported nanofilms not only allows us to test this hypothesized connection but also enables us to probe the exclusive effect of interface proximity on heterogeneous nucleation, in the absence of other competing factors such as contact lines, interfacial curvature, and collision-induced perturbations. In other words, supported films constitute ideal model systems for determining whether nanoscale proximity is sufficient for inducing faster heterogeneous nucleation in contact freezing. As such, we will refer to the strong sensitivity of rate to film thickness as "contact freezing propensity" for brevity, even though contact freezing is a complex phenomenon whose precise kinetics and mechanism is likely affected by a plethora of other factors. Our calculations reveal that nanoscale proximity is indeed a sufficient condition for inducing kinetic enhancements of the types observed in contact freezing experiments, but only for a liquid that is prone to surface freezing. More precisely, heterogeneous nucleation becomes orders of magnitude faster in ultrathin films of the surface-freezing liquid wherein critical nuclei adopt a hourglass-shaped structure due to the nanoscale proximity of the two interfaces, while no dependence of rate on thickness is observed for the other liquid. Our analysis using classical nucleation theory (CNT)[52] reveals that the formation of such nuclei can result in a decrease in nucleation barrier, but not by enough to quantitatively explain the observed increase in rate. We explain this discrepancy by noting that the presence of an INP modulates the free interfacial structure of the films exhibiting faster nucleation, which results in a decrease in the effective contact angle and the nucleation barrier.

METHODS

System Description and Molecular Dynamics Simulations. We consider supported films of two water-like tetrahedral liquids. Both liquids belong to the Stillinger−Weber (SW)[53] family of potentials in which the tetrahedral arrangement of nearest neighbors around a central site is enforced by including in the interatomic potential a three-body term that penalizes deviations from the tetrahedral angle. The magnitude of the energetic penalty is tuned using a parameter called tetrahedrality, λ. The first model liquid is mW,[50] a widely used coarse-grained model of water with $\lambda = 23.15$, which has been shown[9,10] to not undergo surface freezing, while the second liquid is a reparameterized variant of mW with $\lambda = 21$ that undergoes[11] surface freezing. We call this second liquid SW21, which is different from real water and mW in several aspects such as its melting point (206 K for SW21 vs 274 K for mW) and its hydration structure.[11] The precise phase diagrams of these two models can be found elsewhere.[50,54] We choose SW21 over atomistic models with surface freezing propensity—such as TIP4P/Ice[49]—not only due to the prohibitively large computational cost of the latter but also because comparing SW21 and mW allows us to explore the effect of surface freezing propensity on heterogeneous nucleation in two models that are otherwise similar. Conversely, comparing any potential differences between the contact freezing propensities of TIP4P/Ice and mW could not be conclusively attributed to their

https://dx.doi.org/10.1021/jacs.0c10663
J. Am. Chem. Soc. 2021, 143, 2272−2284

differing surface freezing tendencies and could instead be caused by other factors, such as the presence of electrostatic interactions in the TIP4P/Ice system. The temperatures at which rates are computed correspond to similar relative supercoolings (or T/T_m values), which all lie between 0.8 and 0.87. We put liquid films of mW and SW21 (Figure 1d) in contact with two types of model INPs. The first INP is a graphene wall that interacts with liquid molecules via the two-body part of the SW potential, with $\varepsilon^\mathrm{g}_\mathrm{mW} = 0.52$ kcal mol^{-1} and $\varepsilon^\mathrm{g}_\mathrm{SW21} = 0.13$ kcal mol^{-1} for mW and SW21, respectively. $\varepsilon^\mathrm{g}_\mathrm{mW}$ is adopted from Bi et al.,[55] while $\varepsilon^\mathrm{g}_\mathrm{SW21}$ is chosen because no heterogeneous nucleation was observed for $\varepsilon^\mathrm{g}_\mathrm{mW}$ in the SW21 system. We use a value of $\sigma^\mathrm{g} = 0.32$ nm for both liquids. (ii) The second INP is a structureless attractive wall interacting via the Lennard-—ones (LJ) 9-3 potential[56] with $\epsilon^\mathrm{LJ}_\mathrm{mW} = 1.2$ kcal mol^{-1} and $\sigma^\mathrm{LJ}_\mathrm{mW} = 0.32$ nm, and $\epsilon^\mathrm{LJ}_\mathrm{SW21} = 0.48$ kcal mol^{-1} and $\sigma^\mathrm{LJ}_\mathrm{SW21} = 0.3$ nm for mW and SW21, respectively. These values represent the smallest ε values for which heterogeneous nucleation is observed in conventional 50 ns long MD simulations at 215 and 155 K in the mW and SW21 systems, respectively. All LJ 9-3 interactions were truncated at 2.5σ.

All MD simulations are performed in the canonical (NVT) ensemble using the large-scale atomic/molecular massively parallel simulator (LAMMPS)[57] package. Equations of motion are integrated using the velocity-Verlet algorithm with a time step of 5 fs, while the temperature is controlled using the Nosé−Hoover[58,59] thermostat with a time constant of 0.5 ps. Supercooled liquid configurations are prepared by melting a properly sized film of cubic ice at 350 and 250 K for mW and SW21 systems, respectively. We collect a minimum of 100 melted configurations once every 0.05 ns and gradually quench them to the respective target temperature at a cooling rate of 6.25 ps K^{-1}. This choice was guided by the fact that structural relaxation times for both mW and SW21 never exceed 2 ps within the range of temperatures considered in this work (Figure S1). Therefore, the quenched configurations have sufficient time to structurally relax during cooling and did not get kinetically arrested. Note that the ensuing films are sandwiched between the INP and the vapor phase, which, due to the low vapor pressure of mW-like models under supercooled conditions,[60] is technically indistinguishable from vacuum. This implied simulating nucleation at zero pressure, which accurately represents atmospherically relevant conditions. All system characteristics (including system sizes) are given in Table S1.

Rate Calculations. Nucleation rates are computed using our recently developed jFFS algorithm[51] with the number of molecules within the largest crystalline nucleus as the order parameter, $\xi(\cdot)$. Individual molecules are classified as solid-like or liquid-like on the basis of the q_6 Steinhart bond order parameter,[61] and the solid-like molecules within a distance cutoff r_c are clustered to form crystalline nuclei. In order to be consistent with our earlier work on the SW21 model,[11] we use $r_\mathrm{c} = 0.32$ and 0.345 nm for mW and SW21, respectively, and apply the chain exclusion algorithm of Reinhardt et al.[62] Further details about the particular definition of q_6 and the clustering algorithm can be found in our earlier publications.[10,11] Forward flux sampling (FFS)[63] has been extensively utilized for studying rare events,[64] and jFFS is a generalized variant of FFS particularly suitable for use with order parameters—such as that utilized in this work—that undergo high-frequency high-amplitude temporal fluctuations. The rate of transition from the supercooled liquid basin $A = \{\mathbf{x}{:}\xi(\mathbf{x}) < \xi_A\}$ to the crystalline basin $B = \{\mathbf{x}{:}\ \xi(\mathbf{x}) \geq \xi_B\}$ is estimated by partitioning the intermediate $[\xi_A, \xi_B)$ region using N milestones $\xi_A < \xi_0 < \cdots < \xi_N = \xi_B$, which are level sets of $\xi(\cdot)$ and by recursively computing the flux of trajectories leaving A and reaching each milestone. This is achieved by computing the flux of trajectories crossing ξ_0 (computed from long conventional MD trajectories within A) and estimating transition probabilities between successive milestones (by initiating trial trajectories from configurations arising from earlier crossings). The mechanism of nucleation is characterized using the pedigree analysis method described in ref 65. Further details about jFFS calculations can be found in Section S3 in the Supporting Information.

RESULTS AND DISCUSSION

Kinetics and Mechanism of Nucleation. We first explore the dependence of heterogeneous nucleation rate on the thickness of the supported film, which is a measure of the proximity of the INP and the free interface. As depicted in Figure 1e, the rate is virtually insensitive to film thickness in the mW system, which does not undergo surface freezing. Note that such a lack of sensitivity is not an artifact of the relatively large nucleation rates at 235 K and is also observed at 240 K, where nucleation rates are 4 orders of magnitude smaller. In the SW21 system, which undergoes surface freezing, however, the rate is very sensitive to film thickness, as can be seen in Figure 1f, and is almost 6 orders of magnitude larger in the ultrathin 1.2 nm thick film than in thicker films. These findings confirm our core hypothesis that there is a relationship between the ability of a free interface to enhance homogeneous and heterogeneous nucleation, as the contact freezing propensities of these two liquids match their respective surface freezing tendencies. We use the heuristics developed in our earlier publication[66] to show that these findings are not affected by finite size effects, with the results of such an analysis being presented in Figure S2 and Table S2. This is further confirmed by conducting MD simulations of the 1.2 nm film in a larger simulation box (Figure S3) with the rate obtained from the mean first passage time method[67] being almost identical with that reported in Figure 1f. Also, these rates are tens of orders of magnitude larger than the homogeneous nucleation rates at identical temperatures (Table S3).

In order to understand the origin of this contrasting behavior, we inspect the nucleation mechanism by analyzing the spatial spread of the largest crystalline nuclei in "surviving" configurations. A configuration stored at an FFS milestone is called surviving if it bears progeny at the target crystalline basin: i.e., if at least one configuration at ξ_N can be traced back to it via a collection of trial trajectories. As can be seen in Figure 2, a major qualitative difference is observed between the ultrathin SW21 film and the remaining films. While the crystalline nuclei only form at the graphene surface in mW films of all thicknesses (Figure 2c,d and Figure S4c,d) and in thicker SW21 films (Figure 2b and Figure S4a,b), they tend to emerge at either of the two interfaces in the ultrathin SW21 film (as can be seen from the representative surviving configurations and pathways depicted in Figure S5) and grow to form hourglass-shaped nuclei. (Here, by "hourglass" we refer to a structure that is fatter at the top and the bottom than in the middle.) Representative critical nuclei depicted in the insets are also hourglass-shaped in the ultrathin SW21 film (Figure 2a and Figures S3 and S5) as opposed to spherical cap-like nuclei reminiscent of classical heterogeneous nucleation in thicker films (Figure 2b). In mW films, however, all such nuclei are spherical cap-like irrespective of film thickness, as depicted in Figure 2c,d. In particular, nucleation exclusively starts at the graphene wall in ultrathin mW films (Figure 2c), as demonstrated in the pathway depicted in Figure S6.

Clearly, the dependence of mechanism on film thickness follows the same trend as that of the nucleation rate. Most notably, the dramatic enhancement in nucleation kinetics in ultrathin SW21 films is accompanied by an abrupt change in the shape and spatial spread of the crystalline nuclei. This change demonstrates a synergy between the two interfaces in the ultrathin film, which is likely responsible for faster nucleation presumably due to a decrease in the nucleation

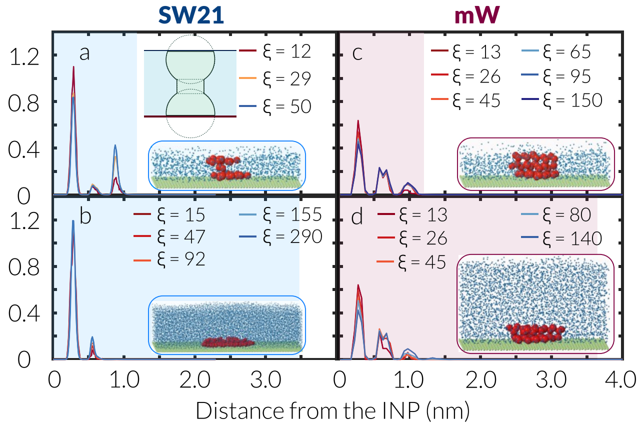

Figure 2. Geometric spread of crystalline nuclei in graphene-supported films. Histograms of the *z* coordinates of the molecules belonging to the largest crystalline nuclei in surviving configurations of SW21 (a, b) and mW (c, d) films at 170 and 235 K, respectively. The area under each histogram is normalized to unity. Legends correspond to surviving nuclei at different jFFS milestones. Insets depict representative critical nuclei in each system, with solid-like molecules within the nuclei, liquid-like molecules, and carbon atoms depicted in red, dark blue, and light green, respectively. Nuclei in (a) are hourglass-shaped with their typical geometry depicted in the inset. Shaded regions correspond to the geometric spreads of the supported films.

barrier. We use the FFS-MFPT method[68] to compute nucleation barriers in SW21 films and observe that the nucleation barrier decreases abruptly upon decreasing the film thickness to 1.2 nm (Figure 3a). We refer to this effect as *interfacial synergy*, since the proximity of the two interfaces leads to increases in rate (and decreases in the nucleation barrier) that are otherwise impossible in the presence of the isolated individual interfaces. We also observe further manifestation of this synergy by noting that surviving configurations at ξ_0 are more likely than vanishing configurations to possess strong free interfacial peaks, as depicted in Figure S7a.

CNT-Based Theoretical Model. In order to determine whether it is the formation of hourglass-shaped nuclei that results in a decrease in the nucleation barrier, we employ the formalism of classical nucleation theory,[52] which has been extensively utilized to interpret the findings of experimental and computational studies of nucleation.[69] In the standard form of CNT for heterogeneous nucleation, crystalline nuclei are assumed to be spherical caps that form at the surface that harbors nucleation and grow at a fixed three-phase contact angle. This results in a nucleation barrier given by

$$\Delta G^*_{\mathrm{het}} = \frac{16\pi\gamma_{\mathrm{sl}}^3 f_{\mathrm{c}}(\theta)}{3\rho_{\mathrm{s}}^2|\Delta\mu|^2} \tag{1}$$

wherein $\Delta\mu$ is the chemical potential difference between the supercooled liquid (l) and the crystal (s), γ_{sl} is the solid−liquid surface tension, ρ_{s} is the number density of the crystal, and θ is the three-phase contact angle. $f_{\mathrm{c}}(\theta)$—given by eq S7 in the Supporting Information—is a measure of the efficiency of heterogeneous nucleation and is called the potency factor[70]—or the compatibility factor.[71] We generalize this standard form of CNT to the case of two parallel interfaces separated by a distance l by assuming that crystalline nuclei can comprise two—intersecting or nonintersecting—spherical caps of radii r_{w} and r_{f} forming at the INP wall (w) and the free interface (f), respectively, and can be further connected via a cylindrical bridge of radius r_{c}. Within this framework, nucleation can start at both interfaces, commensurate with our observations in ultrathin SW21 films. Moreover, model nuclei can only touch each interface at a fixed contact angle (θ_{w} for the INP and θ_{f} for the free interface). This further limits the set of permissible values of r_{w}, r_{f}, and r_{c}, as each cap can intersect the opposing interface only within the base of the opposing cap, and the cylindrical bridge will also have to be contained within those bases or not touch the interfaces at all. (See Section S1B in the Supporting Information for a detailed discussion.) The free energy of formation of such a composite nucleus (Figure 3b) will thus be given by

$$\Delta G^{l}_{\mathrm{hg}}(r_{\mathrm{w}}, r_{\mathrm{f}}, r_{\mathrm{c}}) = \sum_{i\in\{\mathrm{w,f}\}} \pi r_i^2(\gamma_{i\mathrm{s}} - \gamma_{i\mathrm{l}})\sin^2\theta_i - V_{\mathrm{hg}}\,\rho_{\mathrm{s}}|\Delta\mu| + \gamma_{\mathrm{sl}} S_{\mathrm{hg}} \tag{2}$$

with V_{hg} and S_{hg} being the volume and the liquid-exposed surface area of the hourglass-shaped nucleus, respectively, and $\gamma_{\alpha\beta}$ the surface tension between phases α and $\beta \in${w,f,l,s}. The free energy of formation of a nucleus of size N will thus be given by

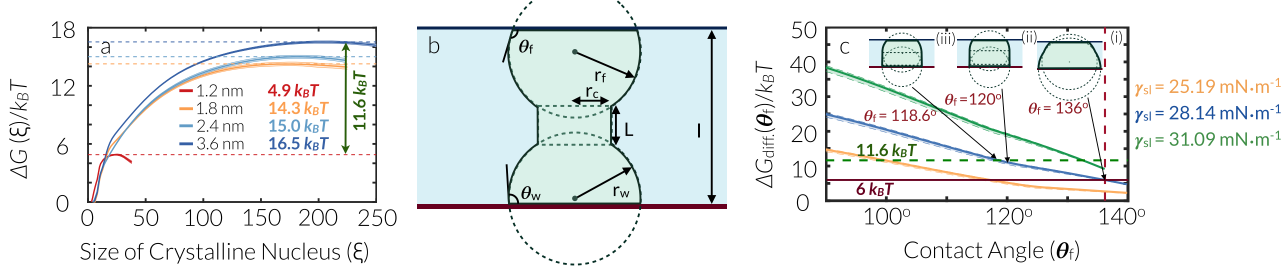

Figure 3. CNT-based theoretical description of nucleation. (a) Free energy profiles computed using the FFS-MFPT method[68] for nucleation within graphene-supported SW21 films. (b) Schematic representation of an hourglass-shaped crystalline nucleus. θ_{w} and θ_{f} are the corresponding contact angles at the INP and the free interface, respectively, while l is the thickness of the film. (c) ΔG_{diff} vs θ_{f} for the γ_{sl} value given in ref 11 (blue). The orange and green curves are computed at the boundaries of the 95% confidence interval of γ_{sl}, while each dotted curve is computed at $\theta_{\mathrm{w}} \pm \delta\theta_{\mathrm{w}}$ with $\delta\theta_{\mathrm{w}}$ being the error bar in θ_{w}. The shade around each curve is therefore a measure of uncertainty in ΔG_{diff} at a fixed γ_{sl} due to uncertainties in θ_{w}. The insets depict representative nucleus shapes predicted from the theory. The dark red and dark green horizontal lines correspond to the ΔG_{diff} values predicted from CNT for the uncorrected θ_{f} and estimated from the FFS-MFPT method, respectively.

$$\Delta G^{l}_{\mathrm{hg}}(N) = \min_{\rho_{\mathrm{s}} V_{\mathrm{hg}}(r_{\mathrm{w}}, r_{\mathrm{f}}, \mathrm{r}_c) = N} \Delta G^{l}_{\mathrm{hg}}(r_{\mathrm{w}}, r_{\mathrm{f}}, r_{\mathrm{c}}) \tag{3}$$

The nucleation barrier $\Delta G^{l,*}_{\mathrm{hg}}$ can be estimated by maximizing $\Delta G^{l}_{\mathrm{hg}}(N)$. If the corresponding critical nucleus is comprised of only a single spherical cap, i.e., with $r_{\mathrm{w}} \neq 0$ and $r_{\mathrm{f}} = r_{\mathrm{c}} = 0$, $\Delta G^{l,*}_{\mathrm{hg}}$ will be identical to $\Delta G^{*}_{\mathrm{het}}$ given by eq 1 and the proximity of two interfaces will not result in smaller barriers and faster nucleation. One can therefore use $\Delta G_{\mathrm{diff}} = \Delta G^{*}_{\mathrm{het}} - \Delta G^{l,*}_{\mathrm{hg}}$ as a measure of the efficacy of the second interface in enhancing nucleation.

Before discussing the predicted ΔG_{diff} values, we first give an overview of how we estimate the necessary thermodynamic parameters. Unlike quantities such as $\Delta\mu$ and ρ_{s} that can be accurately estimated via thermodynamic integration and NpT MD simulations, surface tensions and contact angles are extremely difficult to estimate directly in the supercooled regime. For mW-like liquids, indirect estimates based on CNT reveal that γ_{sl} is not very sensitive to temperature[72] or tetrahedrality.[11] We therefore use the value of $\gamma_{\mathrm{sl}} = 28.14 \pm 2.95$ mN m^{-1} reported in ref 11, which satisfactorily describes nucleation in mW-like liquids over a wide range of tetrahedralities. In order to estimate contact angles, we invoke a CNT prediction that has been previously validated in computational studies of heterogeneous ice nucleation on graphene[70] and stipulates that the potency factor is equal to the ratio of the sizes of critical nuclei in heterogeneous and homogeneous nucleation. We consider nucleation in freestanding films and supported 3.6 nm films as references for determining θ_{f} and θ_{w}, respectively, with further details being given in Section S2A in the Supporting Information. We compute $\Delta G^{l}_{\mathrm{hg}}(N)$ for SW21 films of different thicknesses (Figure S8) using the numerical approach described in Section S1D in the Supporting Information and observe that $\Delta G^{l,*}_{\mathrm{hg}}$ is identical with $\Delta G^{*}_{\mathrm{het}}$ in thicker films and is only $6k_{\mathrm{B}}T$ smaller in the ultrathin 1.2 nm film. The corresponding critical nucleus—(i) in the inset of Figure 3c—is comprised of two intersecting spherical caps, as no cylindrical bridge is geometrically possible due to the sizes of the spherical caps. These predictions are qualitatively consistent with the rates and mechanisms obtained from jFFS and demonstrate that the synergy between the two proximal interfaces *can* result in faster nucleation. In mW films, however, $\Delta G^{l,*}_{\mathrm{hg}} = \Delta G^{*}_{\mathrm{het}}$ for films of all thicknesses due to the lack of surface freezing propensity at the free interface.

Structural Characterization of the Free Interface in the Supercooled Liquid. Our theoretical description provides a qualitative explanation for faster nucleation in ultrathin SW21 films. Its quantitative accuracy, however, is limited, as it underestimates the extent by which nucleation is enhanced: i.e., a $6k_{\mathrm{B}}T$ decline in barrier vs the $11.6k_{\mathrm{B}}T$ obtained from the FFS-MFPT method and depicted in Figure 3a. As can be seen from Table S4, such discrepancies cannot be fully explained by uncertainties in model parameters such as surface tensions and contact angles; thus they are caused by either limitations of CNT or peculiarities specific to SW21 ultrathin films. In order to identify—or rule out the existence of—such peculiarities, we analyze the molecular structure of the free interfaces in supported and freestanding liquid films of SW21 and mW. Here, "free interface" corresponds to parts of the film within the last major peak of $\rho(z)$, the density profile as a function of z, the distance from the wall, and the film center for supported and freestanding films, respectively. ($\rho(z)$ profiles for all the films considered in this work are depicted in Figure S9.) We also compute each structural feature within the "bulk" region, i.e. the parts of the films where density is constant and is equal to the bulk value, e.g. at the center of freestanding films. We first compute $g(r,z)$, the planar radial distribution function (RDF),[73] which provides a radially averaged picture of a molecule's hydration shells. As can be noted in Figure 4a, there is a statistically significant difference between free interfacial RDFs of supported and freestanding ultrathin films of SW21, with the supported film RDF possessing a shallower first valley and a weaker second peak, corresponding to more intermixing of the first and second hydration shells in the free interface. Moreover, the free interfacial RDF in the supported ultrathin film lies between those in the bulk and the freestanding film. This suggests that the free interface becomes more bulklike due to its proximity to the graphene wall. The distinction between the free interfacial RDFs of supported and freestanding films disappears in thicker SW21 films (Figure 4b and Figure S4e,f) and in mW films of all thicknesses (Figure 4c,d and Figure S4g,h).

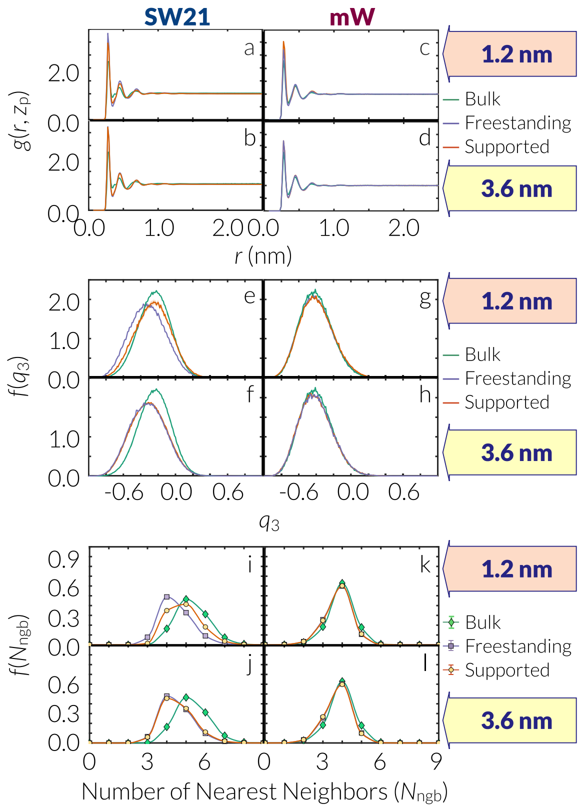

Figure 4. Structural characterization of the free interface. (a−d) Planar RDFs and (e−h) q_3 and (i−l) nearest neighbor count distributions for molecules within the free interfacial regions of supported and freestanding thin films of SW21 (a, b, e, f, i, j) and mW (c, d, g, h, k, l). The "bulk" refers to the properties computed in the central bulklike region of a 3.6 nm thick freestanding film. Error bars in (a−d) and (i−l) are thinner than the curves and smaller than the symbols, respectively. The areas under the curves in (e−h) are normalized to unity, and the shades correspond to error bars.

In order to further probe the structure of the free interface, we compute the q_3 distribution for the molecules within the free interface. q_3 is a local Steinhardt bond order parameter[61] usually used for distinguishing ice polymorphs[74] but is, in general, a measure of how neighbors of a central molecule are oriented within its first hydration shell. Similar to RDFs, free interfacial q_3 distributions differ considerably between supported and freestanding ultrathin SW21 films, as depicted in Figure 4e, while no such difference is observed in thicker SW21 films (Figure 4f and Figure S4i,j) and in mW films of all thicknesses (Figure 4g,h and Figure S4k,l). The rightward shift in q_3 makes free interfaces in supported ultrathin films more bulk-like, a trend also observed for RDFs (Figure 4a). Interestingly, this dramatic change in the q_3 distribution can be fully attributed to a change in the number of molecules within the first hydration shell, as depicted in Figure 4i. Indeed, the q_3 distribution undergoes a rightward shift when the number of molecules within the first hydration shell increases (Figure S10). Again, no change in the nearest neighbor count distribution is observed in thicker SW21 films (Figure 4j and Figure S4m,n) and mW films of all thicknesses (Figure 4k,l and Figure S4o,p). One might expect the synergy between the two interfaces to also result in a change in the structure of the graphene-adjacent interfacial region: i.e., the region corresponding to the first density peak in Figure S9a. Our analysis, however, reveals no such structural modulation, as is evident from planar RDFs and q_3 and nearest neighbor count distributions depicted in Figure S11.

All of these structural features point to the same picture, a free interface that becomes increasingly bulklike in the presence of a proximal INP. Such changes in structure will inevitably alter interfacial properties such as $\gamma_{\rm lv}$ and $\theta_{\rm f}$. In particular, we expect $\gamma_{\rm lv}$ to only increase upon an INP-induced structural modulation, since the unperturbed free interface adopts the structure that minimizes the free energetic penalty associated with forming a two-phase interface. Any deviation from such an "optimal" structure will only increase such a enalty. According to the Young equation, $\theta_{\rm f}$ is related to $\gamma_{\rm lv}$ by $\cos\theta_{\rm f} = (\gamma_{\rm lv} - \gamma_{\rm sv})/\gamma_{\rm sl}$ and will therefore decrease upon an increase in $\gamma_{\rm lv}$. This is based on the reasonable assumption that $\gamma_{\rm sv}$ is not affected by the thinness of the film. Unfortunately, we cannot accurately estimate the perturbed $\gamma_{\rm lv}$ using standard methods such as integrating the difference between normal and lateral stress and the capillary wave method[75] due to the absence of a well-defined bulk region, nor can we compute it using the test area method,[76] which will require straining the crystalline graphene wall. We therefore only examine the sensitivity of $\Delta G_{\rm diff}$ to $\theta_{\rm f}$. As depicted in Figure 3c, $\Delta G_{\rm diff}$ increases upon decreasing $\theta_{\rm f}$ from its unperturbed value of ∼136°. Indeed, decreasing $\theta_{\rm f}$ by ∼18° brings $\Delta G_{\rm diff}$ up to the 11.6 $k_{\rm B}T$ value, depicted in Figure 3a. Moreover, the "perturbed" value of $\theta_{\rm f} \approx 118.6°$ results in critical nucleus shapes and sizes more commensurate with those obtained from jFFS. For instance, unlike the original nucleus (predicted for the original $\theta_{\rm f} \approx 136°$) that is only comprised of two spherical caps, all critical nuclei for $\theta_{\rm f} \leq 120.6°$ also comprise a cylindrical bridge and therefore more resemble the hourglass-shaped nuclei observed in simulations. Furthermore, with the "corrected" $\theta_{\rm f} \approx 118.6°$, the critical nucleus size is predicted to be $N^*_{\rm corr} \approx 150^{+146}_{-75}$, which is considerably smaller than $N^* \approx 216^{+113}_{-79}$ (predicted for $\theta_{\rm f} \approx 136°$) and is closer to the average critical nucleus size of $N^*_{\rm jFFS} \approx 31 \pm 2$ obtained from jFFS. Note that the difference between $N^*_{\rm corr}$ and $N^*_{\rm jFFS}$ might be inflated, as the apparent nucleus size determined from classical MD or jFFS is usually very sensitive to the employed clustering and classification algorithm.[77] Indeed, analyzing our critical configurations using a second-order parameter in which the first hydration shells of solid-like molecules are included in the nucleus yields an average nucleus size of 92 ± 1, which is considerably closer to $N^*_{\rm corr}$ and falls within its confidence interval. Finally, as can be seen in Figure 3c, our analysis is robust to uncertainties in the model parameters such as $\gamma_{\rm sl}$ even though the "corrected" $\theta_{\rm f}$ that would yield the expected $\Delta G_{\rm diff}$ will be slightly different. The confidence intervals for the "corrected" $\theta_{\rm f}$ and its associated N^* is given in Table S4.

It must be noted that the quantitative accuracy of our CNT-based model is still limited even with an adjusted $\theta_{\rm f}$. Most importantly, the predicted nucleation barriers (for both thick and thin films) are considerably larger than those estimated from the FFS-MFPT method. This discrepancy can arise from, among other things, the strong sensitivity of the nucleation barrier to quantities such as surface tensions and contact angles. For instance, a 10% error in $\gamma_{\rm sl}$ and $\theta_{\rm w}$ can result in as much as 33% and 25% errors in $\Delta G^*_{\rm het}$, respectively. It is indeed plausible that we might be overestimating $\theta_{\rm w}$, as the typical critical nuclei on a 3.6 nm SW21 film (e.g., those depicted in Figure 2b) are too flat to be approximated as spherical caps. Other factors that can affect our contact angle estimates are the classification and clustering criteria utilized for detecting the largest crystalline nucleus, which can result in large changes in the apparent size of the critical nucleus.[77] Despite these limitations, our analysis is still useful, as it demonstrates that the synergy between interfaces and structural modulation of the free interface by an INP can collectively explain the observed acceleration of nucleation in ultrathin SW21 films.

Our structural analysis of the free interface also sheds further light on the unresolved conundrum of why different water models have such distinct surface freezing propensities. For all the structural features highlighted in Figure 4, the interfacial regions in freestanding SW21 films are distinct from the bulk, while for mW films, no difference is observed between the bulk and the free interface. This significant difference between these two otherwise similar models can qualitatively explain their differing surface freezing propensities. In other words, in order for the free interface to harbor nucleation at a faster rate, its structure must be sufficiently different from the bulk.

Structureless Walls. In order to ensure that the observed behavior is not an artifact of the molecular structure of the underlying graphene wall and is truly caused by a synergy between a free interface and a "generic" INP, we explore the kinetics and mechanism of nucleation in thin supported SW21 and mW films in the vicinity of LJ 9-3 structureless walls.[56] A structureless wall exerts no lateral force on the molecules and is therefore incapable of inducing any lateral order within the film. Table 1 summarizes the computed nucleation rates in 1.2- and 3.6-nm thick supported mW and SW21 films. In order to keep the corresponding calculations computationally tractable and devoid of finite size effects, we conduct them at slightly lower temperatures. Similar to the case for graphene-supported

Table 1. Summary of Heterogenous Nucleation Rate, $\mathcal{J}$, in Supported SW21 and mW Films in the Vicinity of an LJ 9-3 Structureless INP[a]

		$\log_{10} \mathcal{J}$ (m^{-2} s^{-1})	
model	T (K)	1.2 nm film	3.6 nm film
SW21	165	22.96 ± 0.26	6.82 ± 0.45
mW	220	20.07 ± 0.08	20.86 ± 0.07

[a] Error bars correspond to 95% confidence intervals.

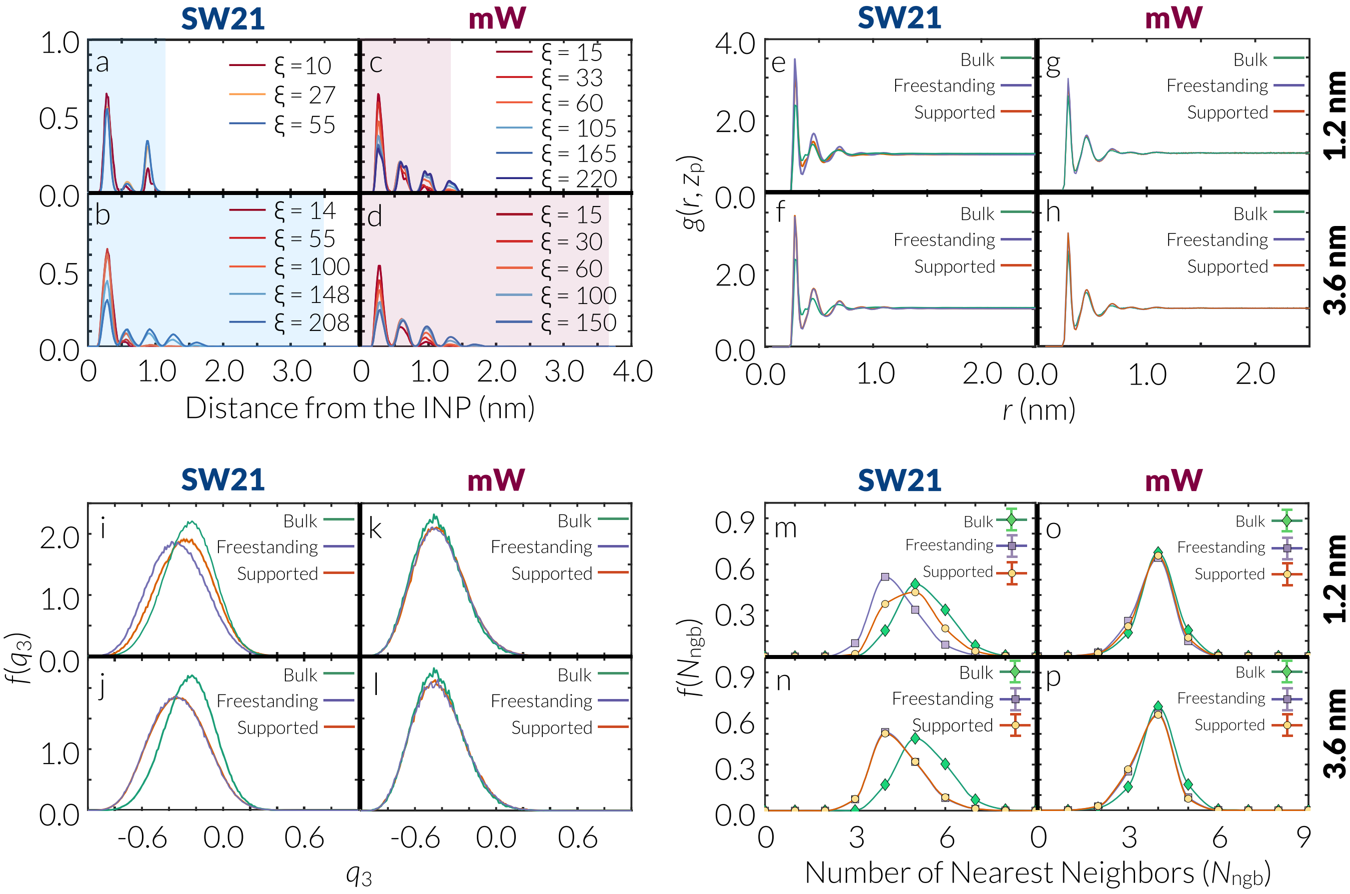

Figure 5. Nucleation mechanism and structural characterization in supported films in the vicinity of a structureless INP. (a−d) Histograms of the z coordinates of the molecules belonging to the largest crystalline nuclei in surviving configurations of SW21 (a, b) and mW (c, d) films. Shaded regions correspond to the geometric spreads of the supported films. (e−h) Planar RDFs and (i−l) q_3 and (m−p) nearest neighbor count distributions for the vapor−liquid interfacial regions of supercooled supported and freestanding films of SW21 and mW. The "bulk" refers to the properties computed in the central bulklike region of a 3.6 nm thick freestanding film. Error bars in (e−h) and (m−p) are thinner than the curves and smaller than the symbols, respectively. The areas under the curves in (i−l) are normalized to unity, and the shades correspond to error bars.

films, the nucleation rate is virtually insensitive to film thickness in the mW system. In the SW21 system, however, nucleation is 16 orders of magnitude faster in the ultrathin film. These findings confirm that even though the extent by which nucleation becomes faster can depend on the particular structure and chemistry of the INP, the mere enhancement in heterogeneous nucleation kinetics only depends on the surface freezing propensity of the corresponding liquid.

We also explore the mechanism of nucleation by quantifying the spatial spread of crystalline nuclei in surviving configurations. In ultrathin SW21 films, crystalline nuclei form at both interfaces and are hourglass-shaped (Figure 5a), a behavior also observed in their graphene-supported counterpart (Figure 2a). Similarly, nucleation proceeds through conventional heterogeneous nucleation in thicker SW21 films (Figure 5b) and in mW films of all thicknesses (Figure 5c,d). Moreover, structureless walls modulate the structure of the free interface in ultrathin SW21 films (Figure 5e,i,m), while no such modulation is observed in thicker SW21 films (Figure 5f,j,n) and mW films of all thicknesses (Figures 5g,h,k,l,o,p).

Applying our CNT-based theory to nucleation near structureless walls is particularly instructive. Since both θ_w and θ_f are obtuse in the case of the structureless wall, a geometric upper bound exists for the sizes of nuclei of the type depicted in Figure 3b. (A rigorous proof is provided in Section S1C in the Supporting Information.) For the unperturbed θ_f, $\Delta G^{\rm l}_{\rm hg}(N)$ is a strictly increasing function of N, and therefore no nucleation is feasible according to the theory. The structural modulation of the free interface, however, implies that θ_f is smaller in supported ultrathin SW21 films. Decreasing θ_f not only makes nucleation possible but also results in a larger $\Delta G_{\rm diff}$ (Figure 6b). Using a perturbed contact angle of ~94.6° yields $\Delta G_{\rm diff} \approx 36k_BT$ obtained from the FFS-MFPT method and depicted in Figure 6a. Similarly to graphene walls, this analysis is robust to uncertainties in model parameters such as $\gamma_{\rm sl}$ and θ_w, as can be seen in Table S4.

Polymorphism and Cubicity of Crystalline Nuclei. Figure 7 depicts the percentage of molecules within the largest crystalline nuclei with local structure of cubic ice, determined using the q_3 order parameter.[74] It is abundantly clear that both INPs favor the formation of hexagonal ice at their immediate vicinity. Consequently, cubicity is very small in the case of graphene-supported SW21 films (Figure 7a), since the crystalline nuclei are predominantly comprised of two layers in thicker SW21 films (Figure 2b and Figure S4a,b). In the 3.6 nm SW21 film supported by the structureless INP, the cubicity is higher, as the crystalline nuclei are comprised of more layers in comparison to their graphene-supported counterparts (Figure 5b). For the ultrathin SW21 films, the cubicity is very small since both interfaces tend to favor the formation of

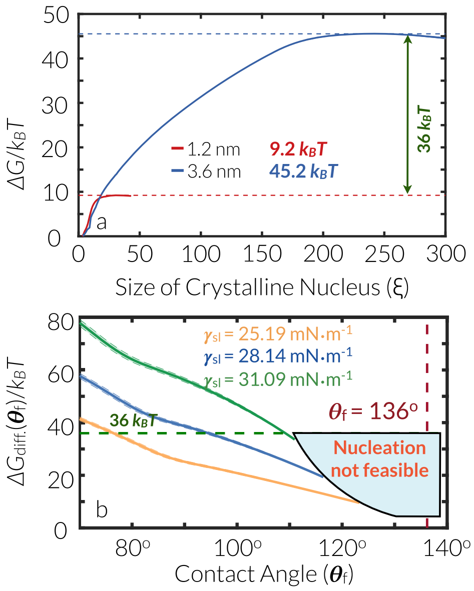

Figure 6. Theoretical analysis of nucleation in the vicinity of a structureless INP. (a) Free energy profiles computed using the FFS-MFPT method[68] for nucleation within supported SW21 films in the vicinity of the structureless INP. (b) ΔG_{diff} vs θ_f for the ultrathin film at the vicinity of the structureless wall for the γ_{sl} value given in ref 11 (blue). The orange and green curves are computed at the boundaries of the 95% confidence interval of γ_{sl}, while each dotted curve is computed at $\theta_w \pm \delta\theta_w$ with $\delta\theta_w$ being the error bar in θw. The shade around each curve is therefore a measure of uncertainty in ΔG_{diff} at a fixed γ_{sl} due to uncertainties in θ_w. Nucleation is not feasible within the light blue region. The dark green horizontal lines corresponds to the ΔG_{diff} values estimated from the FFS-MFPT method in (a).

hexagonal ice. It has indeed been previously shown that free interfaces tend to favor the formation of hexagonal ice motifs in a wide variety of water models, including mW.[12,78] Unlike SW21 films, supported mW films are generally more cubic (Figure 7c,d). While this can be partially attributed to the existence of more layers within the crystalline nuclei (Figures 2c,d and 5c,d and Figure S4c,d), it can also be due to the higher propensity of mW toward stacking disorder. Further studies are needed to assess the sensitivity of polymorphism to the tetrahedrality parameter in the mW-like systems.

Comparison with Experiments. Due to the limited spatiotemporal resolution of the existing experimental techniques, the mechanistic details obtained here cannot be directly verified in experiments. We can, however, compare the kinetic enhancements observed here to those reported in contact freezing experiments. Due to the interfacial nature of heterogeneous nucleation, we report all rates in nucleation events per unit area per unit time. This is in contrast to experiments where an average volumetric nucleation rate is reported for an ensemble of microdroplets. It is therefore necessary to build a kinetic model to convert our areal rates (computed in idealized systems) to the apparent volumetric rates measured in experiments. More specifically, $\mathcal{J}_a(s, \mathbf{\Phi})$, the areal rate of heterogeneous nucleation on an INP will depend on s, its distance from the free interface, and $\mathbf{\Phi}$, its orientation relative to the free interface. The average volumetric nucleation rate for a droplet of radius r_0 with n dispersed INPs will thus be given by

$$\mathcal{J}_v[r_0; p(\cdot)] = \frac{3an}{r_0^3}\int_0^{r_0}\int_{\mathbf{\Phi}} r^2 p(r, \bar{\mathbf{\Phi}})\mathcal{J}_a(r_0 - r, \bar{\mathbf{\Phi}})\, \mathrm{d}\bar{\mathbf{\Phi}}\, \mathrm{d}r \tag{4}$$

where a is the surface area of an individual INP and $4\pi r^2 p(r, \mathbf{\Phi})$ dr d$\mathbf{\Phi}$ is the probability of observing it at a distance r from the center and at a relative orientation $\mathbf{\Phi}$. Both $\mathcal{J}_a(\cdot)$ and $p(\cdot)$ can, in principle, be constructed using a combination of thermodynamic analysis and extensive molecular simulations. Note that eq 4 is only valid if the INPs do not ’”interact” with one another: i.e., that their nanoscale proximity and/or aggregation does not result in faster nucleation.

The simple physical picture emerging from this work suggests that $\mathcal{J}_a$ can take the two distinct values $\mathcal{J}_a^{(s)}$ and $\mathcal{J}_a^{(i)}$ for $s \leq s_0$ and $s > s_0$, respectively, where s_0 is the threshold for transitioning from hourglass-shaped to regular nuclei and $\mathcal{J}_a^{(s)} \gg \mathcal{J}_a^{(i)}$. We also expect the interfacial contribution to eq 4 to be dominated by the orientation in which the INP is parallel to the free interface. This is because an arrangement in which the two interfaces are proximal, but make a nonzero angle, is not mechanically stable and depending on the wetting properties of the INP will either revert to the parallel arrangement or will partially dewet (and form a contact line) over time scales considerably shorter than the nucleation time.

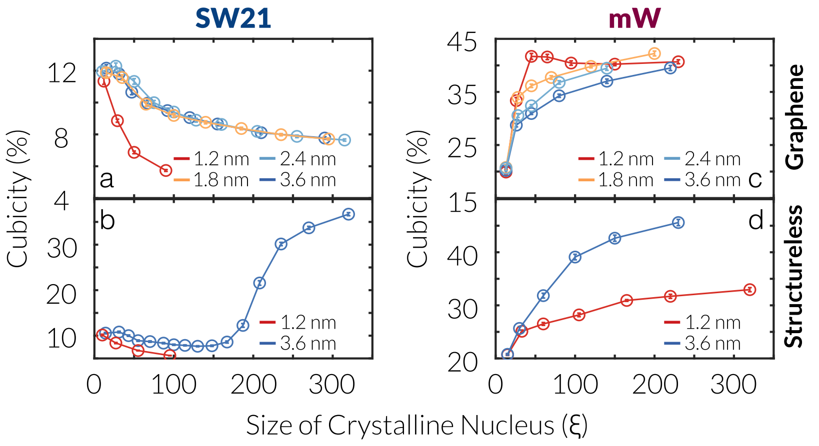

Figure 7. Cubic content of crystalline nuclei. Percentage of solid-like molecules within the crystalline nuclei with the local structure of cubic ice in (a, b) SW21 and (c, d) mW films in the vicinity of (a, c) graphene and (b, d) the structureless INP.

(We do not expect the latter scenario to result in considerable changes in $\mathcal{J}_a^{(s)}$, as contact lines have been shown to not accelerate heterogeneous ice nucleation on chemically uniform surfaces.[40,41]) The only plausible reason for $\mathcal{J}_a^{(s)}$ to be orientation-dependent is if the underlying INP has different crystallographic planes with differing ice-nucleating potencies. Depending on which of these planes comes in contact with the free interface, the extent by which nucleation is enhanced might be different. Due to the simple geometries of the INPs considered in this work (a single layer of graphene and a structureless INP with no crystallographic features), this latter situation is not relevant here. If the INPs are also uniformly distributed within the droplet, the apparent volumetric rate will be given by

$$\mathcal{J}_v^{(u)} = an\mathcal{J}_a^{(i)}(3\alpha\varsigma + 1) \qquad (5)$$

with $\alpha = s_0/r_0 \ll 1$ and $\varsigma = \mathcal{J}_a^{(s)}/\mathcal{J}_a^{(i)} \gg 1$. (The derivation of eq 5 is included in Section S4 in the Supporting Information.) We call $3\alpha\varsigma$ the *enhancement factor*, as it is the factor by which the apparent volumetric rate is enhanced due to "inside-out" freezing, and denote it by χ. According to the calculations conducted here, s_0 is ion the order of a few nanometers, while ς varies between 10^6 and 10^{16}. This will correspond to $3\alpha\varsigma \approx 10^3{-}10^{13}$ for a microdroplet, which is in line with the enhancements observed in earlier experimental studies[30,31] that report enhancements of between 5 and 13 orders of magnitude.

While this simple kinetic model predicts χ values that are in reasonable agreement with experiments, it is important to assess its robustness to violations of some of its key underlying assumptions. In particular, we consider a situation in which $\mathcal{J}_a^{(s)}$ is not constant within the interfacial region ($s \leq s_0$). It must, however, be noted that even then $\mathcal{J}_a^{(s)}$ is unlikely to be an arbitrary continuous function of s. This is because a liquid nanofilm that lies in between an INP and the free interface will be layered as can be seen in Figure S9. Consequently, not only will the thickness of such a film change in increments of 0.3–0.4 nm (the characteristic thickness of each liquid layer) but also $\mathcal{J}_a^{(s)}$ will be a discontinuous function of s and will only depend on the number of liquid layers that separate the INP and the free interface. As demonstrated in detail in Section S4 in the Supporting Information, the enhancement factor obtained from such a stratified model will be dominated by contributions from the ”magic“ separations at which $\mathcal{J}_a^{(s)}/\mathcal{J}_a^{(i)}$ is the largest. This will make our predictions robust to a "worst-case" scenario in which nucleation is only enhanced within a 1.2 nm film (i.e., one comprised of three full liquid layers) and not for films that are thicker or thinner. Under such a scenario, $\mathcal{J}_v(r_0)$ will be dominated by contributions from $s \approx 1.2$ nm, which will eclipse contributions from slow nucleation at other permissible thicknesses. As a result, the enhancement factor will only decrease by an algebraic factor given by eq S34, while its order of magnitude will remain unchanged. Therefore, the enhancement in rate within a 1.2 nm film alone is still sufficient for a dramatic increase in $\mathcal{J}_v$ even if it ditsappears for films with fewer or more liquid layers.

■ CONCLUSION

In this work, we explore how free interfaces affect heterogeneous ice nucleation by computing heterogeneous nucleation rates in supported supercooled nanofilms of two model water-like tetrahedral liquids. We observe that the kinetics of nucleation is enhanced by several orders of magnitude in ultrathin films of the liquid that undergoes surface freezing: i.e., that has a free interface amenable to homogeneous nucleation. No such enhancement is observed for the liquid with no surface freezing propensity. We use classical nucleation theory to conclude that the formation of hourglass-shaped crystalline nuclei (observed in our jFFS simulations of the films that undergo faster nucleation) can result in a considerable decrease in the nucleation barrier, but not by enough to explain the extent of increase in rate. By analyzing the structure of the supercooled liquid, we observe that the INP alters the structure of the free interface in the ultrathin films that undergo faster heterogeneous nucleation and makes it more bulk-like. This results in a decrease in the three-phase contact angle at the free interface, which in turn leads to smaller nucleation barriers and faster nucleation. We confirm these findings for both graphene and model structureless LJ 9-3 walls.

Both model INPs considered in this work induce significant structural perturbations within the free interfacial region of the ultrathin SW21 film, while the INP-adjacent interface is mostly unaffected by the free interface. Note that either of these assertions might be violated for INPs with differing topographies and chemistries. As demonstrated in the case of graphene, faster nucleation can still be possible in the absence of INP-induced structural modulations, but the extent of enhancement will be attenuated considerably. Further studies with a wide variety of INPs are needed to probe whether and when any of these key observations are violated.

Our work provides ample evidence that nanoscale proximity of an INP and a vapor–liquid interface can lead to rate increases commensurate with those observed in contact nucleation. There are, however, reasons to suspect that these findings might have limited direct relevance to atmospheric contact freezing, which occurs under conditions far from equilibrium and is likely affected by a plethora of other factors. Therefore, even though we demonstrate that nanoscale proximity is a sufficient condition for kinetic enhancement in contact nucleation, it is plausible that the inclusion of those other effects might result in comparable (or even larger) increases in the nucleation rate. Further studies are needed to assess the relative importance of factors such as etching,[34] vapor deposition,[35] and mechanical waves.[36] Moreover, the validity of the physical picture presented here is predicated on the assumption that real water undergoes surface freezing, which, while supported by a large body of indirect evidence, has yet to be proven unequivocally.[48]

Recently, pressure perturbations have been proposed[79] as a plausible cause of kinetic enhancement during contact nucleation. According to this theory, a collision between an INP and a water droplet could result in the formation of a distorted contact line and thus lead to the emergence of regions with local negative curvature. The ensuing negative Laplace pressure will then result in faster nucleation due to water's negatively sloped melting curve.[80] While this theory cannot be fully confirmed experimentally due to the difficulties of probing nanoscale local curvature, it tends to perform reasonably well in explaining experimental observations of contact nucleation efficacy. While regions with local negative curvature can arise in our simulations, e.g., due to capillary waves at the free interface, the flat geometry of the supported film makes it extremely unlikely for such regions to extend over sufficiently large swaths of the liquid. Therefore, our work reveals that the emergence of negative pressure is not a necessary condition for faster contact nucleation. Further studies are, however, necessary to probe the combined effects of interfacial curvature and nanoscale proximity on the kinetics and mechanism of heterogeneous nucleation.

Due to the coarse-grained nature of the utilized force fields, our explanation for the relationship between surface and contact freezing is minimal in nature. In particular, we are not able to capture electrostatic and polarizability effects that play an important role in heterogeneous ice nucleation, as demonstrated in several earlier studies.[81−84] Due to the long-range nature of electrostatic interactions, the synergy between an INP with charged or polar groups and the free interface might be stronger and might extend over longer distances. It is therefore likely that the enhancement in nucleation kinetics will occur for films that are considerably thicker than 1 nm. The nature of INP-induced structural modulations might also be different, as the free interface in real water has distinct dielectric signatures due to the presence of dangling hydrogen bonds.[85] Exploring these questions can be the topic of future studies.

Despite the success of our CNT-based theory in predicting faster nucleation in ultrathin SW21 films, its predictive power at a quantitative level is limited due to a confluence of factors, such as the difficulty in accurately estimating interfacial properties such as surface tensions and contact angles and the exponential sensitivity of rate to subtle changes in such quantities. The more important—and consequential—shortcoming of CNT, however, arises from the important role of INP-induced structural modulation that effectively alters the relevant interfacial properties. Therefore, even if all interfacial properties are estimated accurately, and even if CNT accurately describes both homogeneous and heterogeneous nucleation, it will still fall short of accurately predicting the extent by which contact freezing will be faster. This partially explains the quantitative inadequacy of CNT-based models in describing contact freezing in experiments.

We wish to conclude with a few broader implications of this work beyond contact nucleation. First of all, our findings call for a more cautious approach in interpreting immersion nucleation experiments in which a large number of water microdroplets are generated from a mixture of water and INP particles. The fraction of the microdroplets that freeze upon supercooling is then monitored as a function of time, and an average nucleation rate is extracted accordingly.[48] It is totally plausible that the INPs within such droplets might approach the free interfacial region and harbor nucleation at considerably larger rates in accordance with the mechanism discovered in this work. The emergence of such "nucleation hotspots" can, in turn, result in an overestimation of the true immersion nucleation rate, as suggested by eqs 4 and 5. Such nanoscale proximity will be more likely to emerge if the INPs have an intrinsic affinity toward the free interface (e.g., if they are hydrophobic or amphiphilic) or if a droplet has a sufficiently large number of INPs. Indeed, variations in INP concentration among different droplets have already been shown to result in large uncertainties in rate estimates.[27] Our findings suggest that INP-free surface proximity can result in even larger uncertainties, and quantifying its likelihood is critical to obtaining more reliable heterogeneous nucleation rate estimates. The same framework can be used to probe nucleation in other liquids suspected of surface freezing, such as silicon.[86]

Finally, the theoretical approach proposed in this work can be applied to other scenarios in which crystalline nuclei might simultaneously form on multiple interfaces—or interfacial patches—with different chemistries or topographies. This could, for instance, occur in "Janus" slit pores comprised of different types of confining surfaces.[6] A more interesting scenario, however, emerges when a single interface is comprised of multiple distinct "patches", or nanoscale regions with differing chemistries and ice nucleating propensities. Such patchy surfaces can emerge in a wide variety of systems, such as complex organic aerosols,[26] block oligomers[87] and polymers,[88] and ice nucleating[89] and antifreeze[90] proteins. Such patchy surfaces and coatings have garnered increased interest recently due to advancements in various top-down techniques[91] and bottom-up approaches,[92] such as block copolymer self-assembly,[93,94] which have made their precision fabrication possible. In principle, the applicability of the theoretical framework proposed in this work to study nucleation on such patchy surfaces does not depend on their particular chemistries and mechanical and topographical properties. However, such patches sometimes resemble free interfaces, such as hydrophobic patches on a protein,[95] henceforth making the interfacial proximity of the type discussed here even more salient. Our findings demonstrate that different aspects of confinement can be harnessed to realize nonclassical nucleation behavior.

■ ASSOCIATED CONTENT

Supporting Information

The Supporting Information is available free of charge at https://pubs.acs.org/doi/10.1021/jacs.0c10663.

> Further computational details, including the derivation of geometric features of the utilized CNT-based theory, the approach for estimating model parameters and uncertainty analysis, implementation details of jFFS, and further information about the system setup (PDF)

■ AUTHOR INFORMATION

Corresponding Author

Amir Haji-Akbari − *Department of Chemical and Environmental Engineering, Yale University, New Haven, Connecticut 06520, United States;* orcid.org/0000-0002-2228-6957; Email: amir.hajiakbaribalou@yale.edu

Author

Sarwar Hussain − *Department of Chemical and Environmental Engineering, Yale University, New Haven, Connecticut 06520, United States*

Complete contact information is available at: https://pubs.acs.org/10.1021/jacs.0c10663

Notes

The authors declare no competing financial interest.

■ ACKNOWLEDGMENTS

We thank P. G. Debenedetti, T. Koop, V. Molinero, F. Caupin, D. Knopf, A. Michaelides, and G. Sosso for useful discussions. These calculations were performed on the Yale Center for Research Computing. This work used the Extreme Science and Engineering Discovery Environment (XSEDE), which is supported by National Science Foundation grant no. ACI-1548562.[96] A.H.-A. gratefully acknowledges the support of a National Science Foundation CAREER Award (Grant No. CBET-1751971).

■ REFERENCES

(1) Giovambattista, N.; Rossky, P.; Debenedetti, P. Computational studies of pressure, temperature, and surface effects on the structure and thermodynamics of confined water. *Annu. Rev. Phys. Chem.* **2012**, *63*, 179−200.

(2) Takaiwa, D.; Hatano, I.; Koga, K.; Tanaka, H. Phase diagram of water in carbon nanotubes. *Proc. Natl. Acad. Sci. U. S. A.* **2008**, *105*, 39−43.

(3) Han, S.; Choi, M. Y.; Kumar, P.; Stanley, H. E. Phase transitions in confined water nanofilms. *Nat. Phys.* **2010**, *6*, 685−689.

(4) Agrawal, K. V.; Shimizu, S.; Drahushuk, L. W.; Kilcoyne, D.; Strano, M. S. Observation of extreme phase transition temperatures of water confined inside isolated carbon nanotubes. *Nat. Nanotechnol.* **2017**, *12*, 267.

(5) Gao, Z.; Giovambattista, N.; Sahin, O. Phase diagram of water confined by graphene. *Sci. Rep.* **2018**, *8*, 6228.

(6) Kumar, H.; Dasgupta, C.; Maiti, P. K. Phase transition in monolayer water confined in Janus nanopore. *Langmuir* **2018**, *34*, 12199−12205.

(7) Jantsch, E.; Weinberger, C.; Tiemann, M.; Koop, T. Phase transitions of ice in aqueous salt solutions within nanometer-sized pores. *J. Phys. Chem. C* **2019**, *123*, 24566−24574.

(8) Vrbka, L.; Jungwirth, P. Homogeneous freezing of water starts in the subsurface. *J. Phys. Chem. B* **2006**, *110*, 18126−18129.

(9) Li, T.; Donadio, D.; Galli, G. Ice nucleation at the nanoscale probes no man's land of water. *Nat. Commun.* **2013**, *4*, 1887.

(10) Haji-Akbari, A.; DeFever, R. S.; Sarupria, S.; Debenedetti, P. G. Suppression of sub-surface freezing in freestanding thin films of monoatomic water. *Phys. Chem. Chem. Phys.* **2014**, *16*, 25916−25927.

(11) Gianetti, M. M.; Haji-Akbari, A.; Longinotti, M. P.; Debenedetti, P. G. Computational investigation of structure, dynamics and nucleation kinetics of a family of modified Stillinger−Weber model fluids in bulk and free-standing thin films. *Phys. Chem. Chem. Phys.* **2016**, *18*, 4102−4111.

(12) Haji-Akbari, A.; Debenedetti, P. G. Computational investigation of surface freezing in a molecular model of water. *Proc. Natl. Acad. Sci. U. S. A.* **2017**, *114*, 3316−3321.

(13) Campbell, J. M.; Meldrum, F. C.; Christenson, H. K. Observing the formation of ice and organic crystals in active sites. *Proc. Natl. Acad. Sci. U. S. A.* **2017**, *114*, 810−815.

(14) Mascotto, S.; Janke, W.; Valiullin, R. Ice nucleation in periodic arrays of spherical nanocages. *J. Phys. Chem. C* **2017**, *121*, 23788−23792.

(15) Bi, Y.; Cao, B.; Li, T. Enhanced heterogeneous ice nucleation by special surface geometry. *Nat. Commun.* **2017**, *8*, 15372.

(16) Campbell, J. M.; Christenson, H. K. Nucleation- and emergence-limited growth of ice from pores. *Phys. Rev. Lett.* **2018**, *120*, 165701.

(17) Koga, K.; Gao, G.; Tanaka, H.; Zeng, X. C. Formation of ordered ice nanotubes inside carbon nanotubes. *Nature* **2001**, *412*, 802.

(18) Frank, C.; Rao, V.; Despotopoulou, M.; Pease, R.; Hinsberg, W.; Miller, R.; Rabolt, J. Structure in thin and ultrathin spin-cast polymer films. *Science* **1996**, *273*, 912−915.

(19) Swallen, S. F.; Kearns, K. L.; Mapes, M. K.; Kim, Y. S.; McMahon, R. J.; Ediger, M. D.; Wu, T.; Yu, L.; Satija, S. Organic glasses with exceptional thermodynamic and kinetic stability. *Science* **2007**, *315*, 353−356.

(20) Giri, G.; Li, R.; Smilgies, D.-M.; Li, E. Q.; Diao, Y.; Lenn, K. M.; Chiu, M.; Lin, D. W.; Allen, R.; Reinspach, J.; Mannsfeld, S. C. B.; Thoroddsen, S. T.; Clancy, P.; Bao, Z.; Amassian, A. One-dimensional self-confinement promotes polymorph selection in large-area organic semiconductor thin films. *Nat. Commun.* **2014**, *5*, 3573.

(21) Odelius, M.; Bernasconi, M.; Parrinello, M. Two dimensional ice adsorbed on mica surface. *Phys. Rev. Lett.* **1997**, *78*, 2855.

(22) Kimmel, G. A.; Matthiesen, J.; Baer, M.; Mundy, C. J.; Petrik, N. G.; Smith, R. S.; Dohnálek, Z.; Kay, B. D. No confinement needed: Observation of a metastable hydrophobic wetting two-layer ice on graphene. *J. Am. Chem. Soc.* **2009**, *131*, 12838−12844.

(23) Xu, K.; Cao, P.; Heath, J. R. Graphene visualizes the first water adlayers on mica at ambient conditions. *Science* **2010**, *329*, 1188−1191.

(24) Zheng, Y.; Su, C.; Lu, J.; Loh, K. P. Room-temperature ice growth on graphite seeded by nano-graphene oxide. *Angew. Chem.* **2013**, *125*, 8870−8874.

(25) Herbert, R. J.; Murray, B. J.; Dobbie, S. J.; Koop, T. Sensitivity of liquid clouds to homogenous freezing parameterizations. *Geophys. Res. Lett.* **2015**, *42*, 1599−1605.

(26) Knopf, D. A.; Alpert, P. A.; Wang, B. The role of organic aerosol in atmospheric ice nucleation: a review. *ACS Earth Space Chem.* **2018**, *2*, 168−202.

(27) Knopf, D. A.; Alpert, P. A.; Zipori, A.; Reicher, N.; Rudich, Y. Stochastic nucleation processes and substrate abundance explain time-dependent freezing in supercooled droplets. *npj Clim. Atmos. Sci.* **2020**, *3*, 1−9.

(28) Rau, W. Über die Wirkungsweise der Gefrierkerne im unterkühlten Wasser. *Z. Naturforsch., A: Phys. Sci.* **1950**, *5*, 667−675.

(29) Durant, A. J.; Shaw, R. A. Evaporation freezing by contact nucleation inside-out. *Geophys. Res. Lett.* **2005**, *32*, L20814.

(30) Shaw, R. A.; Durant, A. J.; Mi, Y. Heterogeneous surface crystallization observed in undercooled water. *J. Phys. Chem. B* **2005**, *109*, 9865−9868.

(31) Fornea, A. P.; Brooks, S. D.; Dooley, J. B.; Saha, A. Heterogeneous freezing of ice on atmospheric aerosols containing ash, soot, and soil. *J. Geophys. Res.* **2009**, *114*, D13201.

(32) Ladino, L.; Stetzer, O.; Lüönd, F.; Welti, A.; Lohmann, U. Contact freezing experiments of kaolinite particles with cloud droplets. *J. Geophys. Res.* **2011**, *116*, D22202.

(33) Hoffmann, N.; Kiselev, A.; Rzesanke, D.; Duft, D.; Leisner, T. Experimental quantification of contact freezing in an electrodynamic balance. *Atmos. Meas. Technol. Discuss.* **2013**, *6*, 3407−3437.

(34) Fletcher, N. H. Other forms of ice. *J. Atmos. Sci.* **1970**, *27*, 49−72.

(35) Cooper, W. A. A possible mechanism for contact nucleation. *J. Atmos. Sci.* **1974**, *31*, 1832−1837.

(36) Fukuta, N. A study of the mechanism of contact ice nucleation. *J. Atmos. Sci.* **1975**, *32*, 1597−1603.

(37) Niehaus, J.; Cantrell, W. Contact freezing of water by salts. *J. Phys. Chem. Lett.* **2015**, *6*, 3490−3495.

(38) Sear, R. P. Nucleation at contact lines where fluid−fluid interfaces meet solid surfaces. *J. Phys.: Condens. Matter* **2007**, *19*, 466106.

(39) Djikaev, Y.; Ruckenstein, E. Thermodynamics of heterogeneous crystal nucleation in contact and immersion modes. *J. Phys. Chem. A* **2008**, *112*, 11677−11687.

(40) Gurganus, C.; Kostinski, A. B.; Shaw, R. A. Fast Imaging of Freezing Drops: No Preference for Nucleation at the Contact Line. *J. Phys. Chem. Lett.* **2011**, *2*, 1449−1454.

(41) Gurganus, C.; Kostinski, A. B.; Shaw, R. A. High-speed imaging of freezing drops: Still no preference for the contact line. *J. Phys. Chem. C* **2013**, *117*, 6195−6200.

(42) Gurganus, C. W.; Charnawskas, J. C.; Kostinski, A. B.; Shaw, R. A. Nucleation at the contact line observed on nanotextured surfaces. *Phys. Rev. Lett.* **2014**, *113*, 235701.

(43) Tabazadeh, A.; Djikaev, Y. S.; Reiss, H. Surface crystallization of supercooled water in clouds. *Proc. Natl. Acad. Sci. U. S. A.* **2002**, *99*, 15873−15878.

(44) Duft, D.; Leisner, T. Laboratory evidence for volume-dominated nucleation of ice in supercooled water microdroplets. *Atmos. Chem. Phys.* **2004**, *4*, 1997.

(45) Ciobanu, V. G.; Marcolli, C.; Krieger, U. K.; Zuend, A.; Peter, T. Efflorescence of ammonium sulfate and coated ammonium sulfate

particles: Evidence for surface nucleation. *J. Phys. Chem. A* **2010**, *114*, 9486−9495.

(46) Kuhn, T.; Earle, M. E.; Khalizov, A. F.; Sloan, J. J. Size dependence of volume and surface nucleation rates for homogeneous freezing of supercooled water droplets. *Atmos. Chem. Phys.* **2011**, *11*, 2853−2861.

(47) Sigurbjornsson, O. F.; Signorell, R. Volume versus surface nucleation in freezing aerosols. *Phys. Rev. E* **2008**, *77*, 051601.

(48) Haji-Akbari, A.; Debenedetti, P. G. Perspective: Surface freezing in water: A nexus of experiments and simulations. *J. Chem. Phys.* **2017**, *147*, 060901.

(49) Abascal, J. L. F.; Sanz, E.; Fernández, R. G.; Vega, C. A potential model for the study of ices and amorphous water: TIP4P/Ice. *J. Chem. Phys.* **2005**, *122*, 234511.

(50) Molinero, V.; Moore, E. B. Water modeled as an intermediate element between carbon and silicon. *J. Phys. Chem. B* **2009**, *113*, 4008−4016.

(51) Haji-Akbari, A. Forward-flux sampling with jumpy order parameters. *J. Chem. Phys.* **2018**, *149*, 072303.

(52) Turnbull, D. Kinetics of heterogeneous nucleation. *J. Chem. Phys.* **1950**, *18*, 198−203.

(53) Stillinger, F. H.; Weber, T. A. Computer simulation of local order in condensed phases of silicon. *Phys. Rev. B: Condens. Matter Mater. Phys.* **1985**, *31*, 5262−5271.

(54) Dhabal, D.; Nguyen, A. H.; Singh, M.; Khatua, P.; Molinero, V.; Bandyopadhyay, S.; Chakravarty, C. Excess entropy and crystallization in Stillinger-Weber and Lennard-Jones fluids. *J. Chem. Phys.* **2015**, *143*, 164512.

(55) Bi, Y.; Cabriolu, R.; Li, T. Heterogeneous ice nucleation controlled by the coupling of surface crystallinity and surface hydrophilicity. *J. Phys. Chem. C* **2016**, *120*, 1507−1514.

(56) Magda, J.; Tirrell, M.; Davis, H. Molecular dynamics of narrow, liquid-filled pores. *J. Chem. Phys.* **1985**, *83*, 1888−1901.

(57) Plimpton, S. J. Fast parallel algorithms for short-range molecular dynamics. *J. Comput. Phys.* **1995**, *117*, 1−19.

(58) Nosé, S. A molecular dynamics method for simulations in the canonical ensemble. *Mol. Phys.* **1984**, *52*, 255−268.

(59) Hoover, W. G. Canonical dynamics: Equilibrium phase-space distributions. *Phys. Rev. A: At., Mol., Opt. Phys.* **1985**, *31*, 1695−1697.

(60) Factorovich, M. H.; Molinero, V.; Scherlis, D. A. A simple grand canonical approach to compute the vapor pressure of bulk and finite size systems. *J. Chem. Phys.* **2014**, *140*, 064111.

(61) Steinhardt, P. J.; Nelson, D. R.; Ronchetti, M. Bond-orientational order in liquids and glasses. *Phys. Rev. B: Condens. Matter Mater. Phys.* **1983**, *28*, 784−805.

(62) Reinhardt, A.; Doye, J. P. K.; Noya, E. G.; Vega, C. Local order parameters for use in driving homogeneous ice nucleation with all-atom models of water. *J. Chem. Phys.* **2012**, *137*, 194504.

(63) Allen, R. J.; Frenkel, D.; ten Wolde, P. R. Forward flux sampling-type schemes for simulating rare events: Efficiency analysis. *J. Chem. Phys.* **2006**, *124*, 194111.

(64) Hussain, S.; Haji-Akbari, A. Studying rare events using forward-flux sampling: Recent breakthroughs and future outlook. *J. Chem. Phys.* **2020**, *152*, 060901.

(65) Haji-Akbari, A.; Debenedetti, P. G. Direct calculation of ice homogeneous nucleation rate for a molecular model of water. *Proc. Natl. Acad. Sci. U. S. A.* **2015**, *112*, 10582.

(66) Hussain, S.; Haji-Akbari, A. How to Quantify and Avoid Finite Size Effects in Computational Studies of Crystal Nucleation: The Case of Heterogeneous Ice Nucleation. *J. Chem. Phys.* **2021**, *154*, 014108.

(67) Wedekind, J.; Strey, R.; Reguera, D. New method to analyze simulations of activated processes. *J. Chem. Phys.* **2007**, *126*, 134103.

(68) Thapar, V.; Escobedo, F. A. Simultaneous estimation of free energies and rates using forward flux sampling and mean first passage times. *J. Chem. Phys.* **2015**, *143*, 244113.

(69) Sosso, G. C.; Chen, J.; Cox, S. J.; Fitzner, M.; Pedevilla, P.; Zen, A.; Michaelides, A. Crystal nucleation in liquids: Open questions and future challenges in molecular dynamics simulations. *Chem. Rev.* **2016**, *116*, 7078−7116.

(70) Cabriolu, R.; Li, T. Ice nucleation on carbon surface supports the classical theory for heterogeneous nucleation. *Phys. Rev. E* **2015**, *91*, 052402.

(71) Alpert, P. A.; Aller, J. Y.; Knopf, D. A. Initiation of the ice phase by marine biogenic surfaces in supersaturated gas and supercooled aqueous phases. *Phys. Chem. Chem. Phys.* **2011**, *13*, 19882−19894.

(72) Espinosa, J. R.; Sanz, E.; Valeriani, C.; Vega, C. Homogeneous ice nucleation evaluated for several water models. *J. Chem. Phys.* **2014**, *141*, 18C529.

(73) Haji-Akbari, A.; Debenedetti, P. G. The effect of substrate on thermodynamic and kinetic anisotropies in atomic thin film. *J. Chem. Phys.* **2014**, *141*, 024506.

(74) Li, T.; Donadio, D.; Russo, G.; Galli, G. Homogeneous ice nucleation from supercooled water. *Phys. Chem. Chem. Phys.* **2011**, *13*, 19807−19813.

(75) Ismail, A. E.; Grest, G. S.; Stevens, M. J. Capillary waves at the liquid-vapor interface and the surface tension of water. *J. Chem. Phys.* **2006**, *125*, 014702.

(76) Gloor, G. J.; Jackson, G.; Blas, F. J.; de Miguel, E. Test-area simulation method for the direct determination of the interfacial tension of systems with continuous or discontinuous potentials. *J. Chem. Phys.* **2005**, *123*, 134703.

(77) Lupi, L.; Hudait, A.; Peters, B.; Grünwald, M.; Mullen, R. G.; Nguyen, A. H.; Molinero, V. Role of stacking disorder in ice nucleation. *Nature* **2017**, *551*, 218−222.

(78) Hudait, A.; Molinero, V. What determines the ice polymorph in clouds? *J. Am. Chem. Soc.* **2016**, *138*, 8958−8967.

(79) Yang, F.; Cantrell, W. H.; Kostinski, A. B.; Shaw, R. A.; Vogelmann, A. M. Is contact nucleation caused by pressure perturbation? *Atmosphere* **2020**, *11*, 1.

(80) Marcolli, C. Ice nucleation triggered by negative pressure. *Sci. Rep.* **2017**, *7*, 1−8.

(81) Yan, J.; Patey, G. Heterogeneous ice nucleation induced by electric fields. *J. Phys. Chem. Lett.* **2011**, *2*, 2555−2559.

(82) Fraux, G.; Doye, J. P. Note: Heterogeneous ice nucleation on silver-iodide-like surfaces. *J. Chem. Phys.* **2014**, *141*, 216101.

(83) Sosso, G. C.; Li, T.; Donadio, D.; Tribello, G. A.; Michaelides, A. Microscopic Mechanism and kinetics of ice formation at complex interfaces: Zooming in on kaolinite. *J. Phys. Chem. Lett.* **2016**, *7*, 2350−2355.

(84) Glatz, B.; Sarupria, S. The surface charge distribution affects the ice nucleating efficiency of silver iodide. *J. Chem. Phys.* **2016**, *145*, 211924.

(85) Du, Q.; Superfine, R.; Freysz, E.; Shen, Y. Vibrational spectroscopy of water at the vapor/water interface. *Phys. Rev. Lett.* **1993**, *70*, 2313.

(86) Li, T.; Donadio, D.; Ghiringhelli, L. M.; Galli, G. Surface-induced crystallization in supercooled tetrahedral liquids. *Nat. Mater.* **2009**, *8*, 726−730.

(87) Biggs, C. I.; Bailey, T. L.; Graham, B.; Stubbs, C.; Fayter, A.; Gibson, M. I. Polymer mimics of biomacromolecular antifreezes. *Nat. Commun.* **2017**, *8*, 1−12.

(88) Jellinek, H.; Kachi, H.; Kittaka, S.; Lee, M.; Yokota, R. Ice releasing block-copolymer coatings. *Colloid Polym. Sci.* **1978**, *256*, 544−551.

(89) Hudait, A.; Qiu, Y.; Odendahl, N.; Molinero, V. Hydrogen-bonding and hydrophobic groups contribute equally to the binding of hyperactive antifreeze and ice-nucleating proteins to ice. *J. Am. Chem. Soc.* **2019**, *141*, 7887−7898.

(90) Haji-Akbari, A. Rating antifreeze proteins: Not a breeze. *Proc. Natl. Acad. Sci. U. S. A.* **2016**, *113*, 3714−3716.

(91) Seo, J.-H.; Park, J. H.; Kim, S.-I.; Park, B. J.; Ma, Z.; Choi, J.; Ju, B.-K. Nanopatterning by laser interference lithography: Applications to optical devices. *J. Nanosci. Nanotechnol.* **2014**, *14*, 1521−1532.

(92) Kim, H.-C.; Park, S.-M.; Hinsberg, W. D. Block copolymer based nanostructures: Materials, processes, and applications to electronics. *Chem. Rev.* **2010**, *110*, 146−177.

(93) Ruiz, R.; Kang, H.; cois, A.; Detcheverry, F.; Dobisz, E.; Kercher, D. S.; Albrecht, T. R.; de Pablo, J. J.; Nealey, P. F. Density multiplication and improved lithography by directed block copolymer assembly. *Science* **2008**, *321*, 936−939.

(94) Luo, M.; Epps, T. H., III Directed block copolymer thin film self-assembly: Emerging trends in nanopattern fabrication. *Macromolecules* **2013**, *46*, 7567−7579.

(95) Pandey, R.; Usui, K.; Livingstone, R. A.; Fischer, S. A.; Pfaendtner, J.; Backus, E. H. G.; Nagata, Y.; Frohlich-Nowoisky, J.; Schmuser, L.; Mauri, S.; Scheel, J. F.; Knopf, D. A.; Poschl, U.; Bonn, M.; Weidner, T.; et al. Ice-nucleating bacteria control the order and dynamics of interfacial water. *Sci. Adv.* **2016**, *2*, No. e1501630.

(96) Towns, J.; Cockerill, T.; Dahan, M.; Foster, I.; Gaither, K.; Grimshaw, A.; Hazlewood, V.; Lathrop, S.; Lifka, D.; Peterson, G. D.; Roskies, R.; Scott, J. R.; Wilkins-Diehr, N. XSEDE: Accelerating scientific discovery. *Comput. Sci. Eng.* **2014**, *16*, 62−74.